REVIEW

Simultaneous PIV–LIF measurements using RuPhen and a color camera

Jiggar Shah[1,2] · Claudio Mucignat[1] · Ivan Lunati[1] · Thomas Rösgen[2]

Abstract

Particle image velocimetry (PIV) and laser-induced fluorescence (LIF) are currently state-of-the-art, non-intrusive measurement techniques that help in our understanding of heat and momentum transfer in thermal fluid flow applications. We present a simplified, integrated PIV–LIF system which simultaneously measures velocity and temperature fields in aqueous flows by means of a novel fluorescent dye (RuPhen), a low-cost continuous-wave diode laser, and a single color camera. We demonstrate that RuPhen is well-suited for this approach due to its peak absorption at 450 nm, peak emission at 605 nm, and a strong temperature-dependent emission with a sensitivity coefficient of 4%/°C. The large Stokes shift between excitation (which also includes Mie scattering of the flow tracers) and the emission facilitates the handling of the signal components in the RGB channels of the camera. To correct the recordings for laser power fluctuations, we propose a novel method that jointly employs two photoluminescence signals. We provide a spectral characterization of the dye at different temperatures and discuss the choice of each component for our measurement system. We demonstrate the potential of our approach by two experimental test cases that focus on thermally driven and turbulent flow regimes.

1 Introduction

As they provide a means to advance our understanding of the coupled heat and momentum transfer in thermal fluid flow applications, numerous studies have focused on non-intrusive measurement techniques that simultaneously quantify velocity and/or temperature fields in experimental fluid dynamics (see, e.g., Yarin 2007; Tagawa et al. 2001; Lavieille et al. 2000; Fujisawa et al. 2005). In this context, particle image velocimetry (PIV Westerweel 1997) and

✉ Claudio Mucignat
claudio.mucignat@empa.ch

Jiggar Shah
shahji@ethz.ch

Ivan Lunati
ivan.lunati@empa.ch

Thomas Rösgen
roesgen@ethz.ch

1 Laboratory for Computational Engineering, Swiss Federal Laboratories for Materials Science and Technology, Ueberlandstrasse 129, 8600 Dübendorf, ZH, Switzerland

2 Institute of Fluid Dynamics, Department of Mechanical and Process Engineering, ETH Zürich, Rämistrasse 101, 8092 Zürich, ZH, Switzerland

laser induced fluorescence (LIF, Walker 1987; Coppeta and Rogers 1998) are whole-field non-intrusive state-of-the-art measurement techniques that have been widely employed to quantify velocity and temperature fields, respectively. PIV measures the velocity field from the displacement of a constellation of tracer particles, while LIF uses temperature-dependent fluorescence to map the emission intensity into temperature.

Whole-field temperature distributions can be measured by recording changes in chrominance (i.e., wavelength) or luminance (i.e., intensity) by using fluorescent dyes or solid particles that are added to the host fluid. If fluorescent solid particles are used, they can also serve as PIV tracers, thereby enabling to simultaneously measure velocity and temperature. These tracers are based either on fluorescence intensity (Vogt and Stephan 2012; Massing et al. 2016; Cellini et al. 2017) or lifetime (phosphorescence, Abram et al. 2016; Massing et al. 2018) that depend on temperature. Particle image thermometry (PIT) is an alternative technique that entails the use of thermochromic liquid crystals (TLCs) that reflect different portions of the visible spectrum depending on temperature (Dabiri 2009). However, the use of PIT tends to be limited by the small temperature range of TLCs and by the dependence of the color response on the angle between illumination and observation.

Although temperature-sensitive particles can be also used as PIV tracers, dissolving fluorescent dyes into the bulk fluid allows experimental measurements characterized by better spatial resolution, lower uncertainty, and a higher temperature range. A previous study employed two non-toxic dyes (uranine, chlorophyll) to perform ratiometric LIF along with PIV measurements (Shah et al. 2018). However, the experimental setup exhibited a considerable complexity due to the use of a pulsed Nd:YAG laser and a minimum of three monochrome cameras (two for ratiometric LIF and one for PIV). This configuration required a pixel-to-pixel mapping of the recordings of all three cameras, as well as the use of beam splitter optics to separate the fluorescence signals, thereby reducing the signal-to-noise ratio. A further limitation was the low absorption of uranine at 532 nm, which required a higher concentration of the dye and higher laser energies for single-shot temperature measurements. Furthermore, the chlorophyll dye was found to be photosensitive and led to considerable signal degradation over time.

To overcome these drawbacks, one could employ two separate signals for velocimetry and thermometry and record them simultaneously by applying a color filter array (CFA, commonly referred to as Bayer filter) to the sensor of a monochrome camera. To our knowledge, only one PIV–LIF study has attempted to simultaneously quantify the velocity and temperature fields in aqueous flows by a similar approach that employed an Ar-ion laser, a color CCD camera, $7\,\mu$m tracer particles, and a two-color/two-dye combination of RhB/Rh110 (Funatani et al. 2004). To obtain the temperature field in a buoyant plume, the ratio of the red/green channels and the tracer displacement in the blue channel were used. However, the temperature sensitivity of the fluorescence signal was found to be 1.7%/°C and to be dependent on the particle seeding density as the particle signature was also recorded by the green pixels due to the typical spectral transmission of the Bayer filters. Moreover, the temperature field was prone to errors arising from to the overlap between the Bayer filter characteristics and the emission spectra of the two dyes.

In this work, we propose an approach to simultaneously perform PIV and LIF by means of a single color camera and a single laser source. This allows us to record both the Mie scattering of fluid tracers and the fluorescence emission of temperature sensitive dyes on a single detector thanks to a RGB Bayer filter. After splitting (or de-bayering) the information of each acquisition into R,G, and B images, we analyze the particle images pairs by means of state-of-the-art PIV algorithms (Raffael et al. 2018) to reconstruct the fluid velocity field. At the same time, the fluorescence signal recorded by one or more color channels can be used to recover the temperature field (Yarin 2007). This approach allows us to reduce the complexity and the cost of the setup by minimizing the number of components.

We base the LIF thermometric measurements on a novel dye, namely RuPhen, which has previously been proposed to obtain precise non-contact temperature measurements in medical applications (Lam et al. 2012). RuPhen belongs to the ruthenium polypyridyl complexes, among which it has the highest temperature sensitivity (Wang et al. 2013). This dye exhibits excellent photostability and has a working range between 273 and 393 K as well as a large Stokes shift.

In the following sections, we explain the technical details of our approach and demonstrate its potential by two experimental test cases that focus on thermally driven and turbulent flow regimes.

2 Methods

In order to optimize the performance of the proposed system, all components must be chosen under a number of operating constraints. Below we describe the selection of the dye, the camera, and the illumination system. We also report the image processing methods as well as the procedure to correct the laser power fluctuations.

2.1 Dye selection

The selection of a suitable fluorescent dye is crucial for the success of the thermometric measurements. Therefore, we first measured the absorption and emission spectra of several temperature-sensitive dyes using a compact spectrometer (Thorlabs CCS200/M). Standard temperature-sensitive dyes (Coppeta and Rogers 1998; Crimaldi 2008) were found unsuitable for our purposes. Rhodamine B (RhB), for instance, has very low absorption below 490 nm, which would require dissolving high concentrations of the dye. Similarly, uranine (FL) has very low temperature sensitivity when excited below 490 nm (Coppeta and Rogers 1998). We also tested natural LIF dyes such as vitamins proposed by Zähringer (2014), but with little success. For those reasons, we selected a water-soluble Ruthenium-based dye (RuPhen, i.e., Tris(1,10-phenanthroline)ruthenium(II) chloride hydrate, CAS No. 207,802-45-7) as alternative dye for LIF thermometry in liquid flows.

RuPhen has previously been used in the form of a temperature-sensitive gel (Lam et al. 2012) and also in temperature sensitive paints (TSPs). It is well suited for our purposes due to its peak absorption at 450 nm (Fig. 1b) and, most important, to a strong temperature dependence of the emission intensity, in particular in the orange/red light spectrum at 550 nm–770 nm (Fig. 1a). Note that RuPhen also exhibits a strong separation between the absorption and the emission wavelengths (Wang et al. 2013). Similar to Rhodamine B, the fluorescence emission of RuPhen decreases with temperature and does not appear to have a temperature-dependent
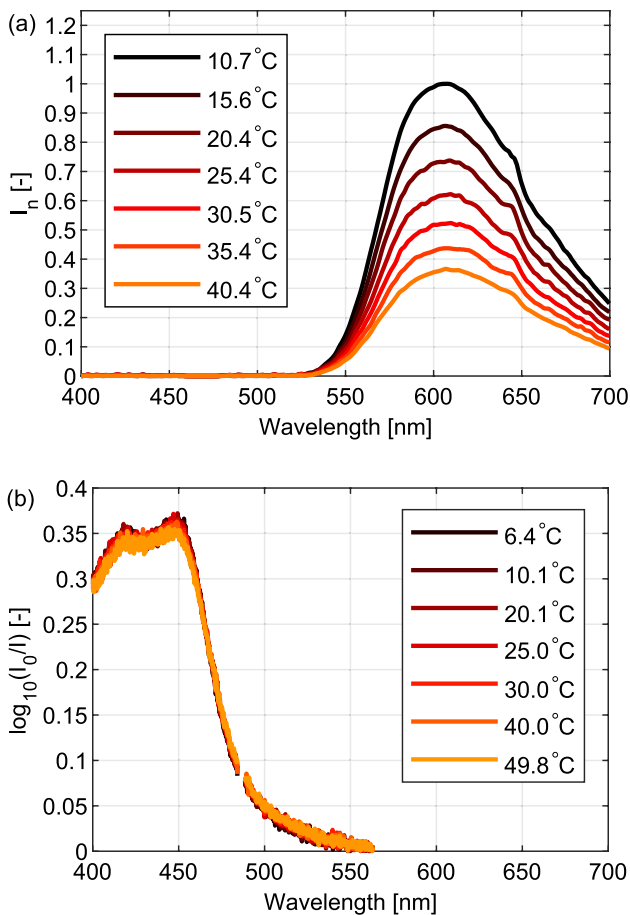
Fig. 1 Emission (**a**) and absorption spectra (**b**) of an aqueous solution with a RuPhen concentration of 19 mg/L at different temperatures

Fig. 2 Temperature sensitivity, s for Rhodamine B and RuPhen over their complete emission spectra

for the specific version of the camera we used, namely a "PCO edge 5.5." This partially restricted the dynamic range of the PIV recordings as we could not lower the separation time Δt between image pairs as the flow velocity increased, thus limiting the measurable flow speeds as in shown in Sect. 3.3. To fully exploit the three RGB channels, we aim at capturing the Mie-scattering of the PIV particles in the blue channel and the temperature-dependent fluorescence emission in the red/green channels of a dye with a peak excitation in the blue channel. Note that by using a single dye but two channels, we are able to avoid the errors arising from the spectral conflicts encountered with multiple dye constellations.

absorption coefficient, $\epsilon(T)$ (Fig. 1b), but rather is its quantum yield $\phi(T)$ most likely varying with temperature. The temperature sensitivity, s (Chaze et al. 2016), of RuPhen was found to be 4%/°C, constant across the spectral region between 550 nm–770 nm, hence, at least more than twice that of RhB (Fig. 2).

2.2 Camera

In recent years, a new generation of global shutter scientific CMOS (sCMOS) sensors has become available, which outperform classical CCD chips in almost all specifications. We use the color version of a sCMOS chip developed by PCO GmbH (along with Fairchild and Andor) that has the advantage of exhibiting very low noise levels, global shutter capability, and a relatively high frame rates in the range 50–100 Hz. The quantum efficiencies of the camera in the different color channels are shown in Fig. 3, along with the absorption and emission spectra of RuPhen. Unfortunately, the "double frame" recording mode, which is very useful in case of extended PIV operation, was not yet available
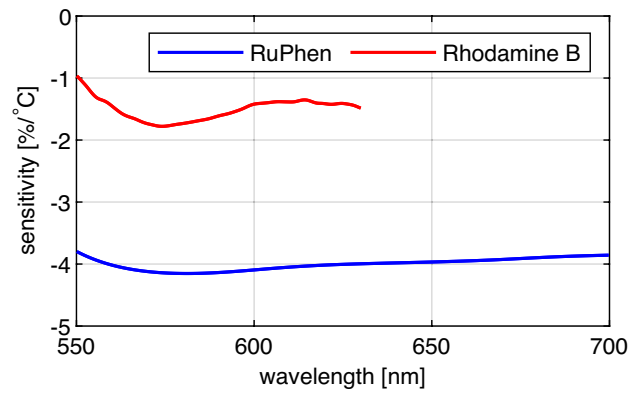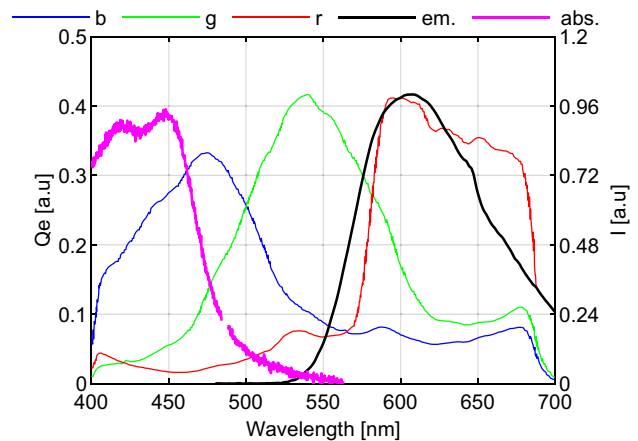

Fig. 3 Spectral sensitivity of the PCO edge5.5 camera, normalized absorption and emission spectra of an aqueous solution with a RuPhen concentration of 19 mg/L

2.3 Laser and illumination

The spectral characteristics of the camera/RuPhen combination require an excitation in the blue wavelength range. As an alternative to a standard pulsed laser, a continuous wave (CW) laser was assembled in-house based on a 3.5 W laser diode module operating at $\lambda_e = 465$ nm (Lasertack GmbH). The laser diode is mounted on a ThermoElectric Cooling (TEC) element and attached to a diode driver/TEC controller. In order to perform volumetric temperature measurements, a scanning mechanism for the laser light sheet was implemented (see Fig. 4). A cylindrical Fresnel lens (LF500-B, $f = 500$ mm, NTKJ Co., Ltd, www.ntkj-japan.com) redirects the small-angle deflections produced by a galvanometer head (Thorlabs GVS 012, scan rate up to a 1 kHz) to render

the laser sheets parallel. Yellow filters ($2 \times$ Schott GG475, transmittance: 2.5% @ 465 nm) are used in front of the camera to avoid overexposing the blue channel and to reduce the leakage into the red/green channels. Images are acquired using an in-house software that synchronizes the laser pulse, the galvo position, and the camera based on a data acquisition device (National Instruments NI-USB-6221).

2.4 Image processing

The images recorded by the camera are saved in 16-bit raw format, from which the red/green/blue pixels are extracted to obtain three RGB images at reduced spatial resolution, as shown in Fig. 5. Notice that the two "green" pixels in the Bayer pattern's unit cell are averaged. Furthermore, no
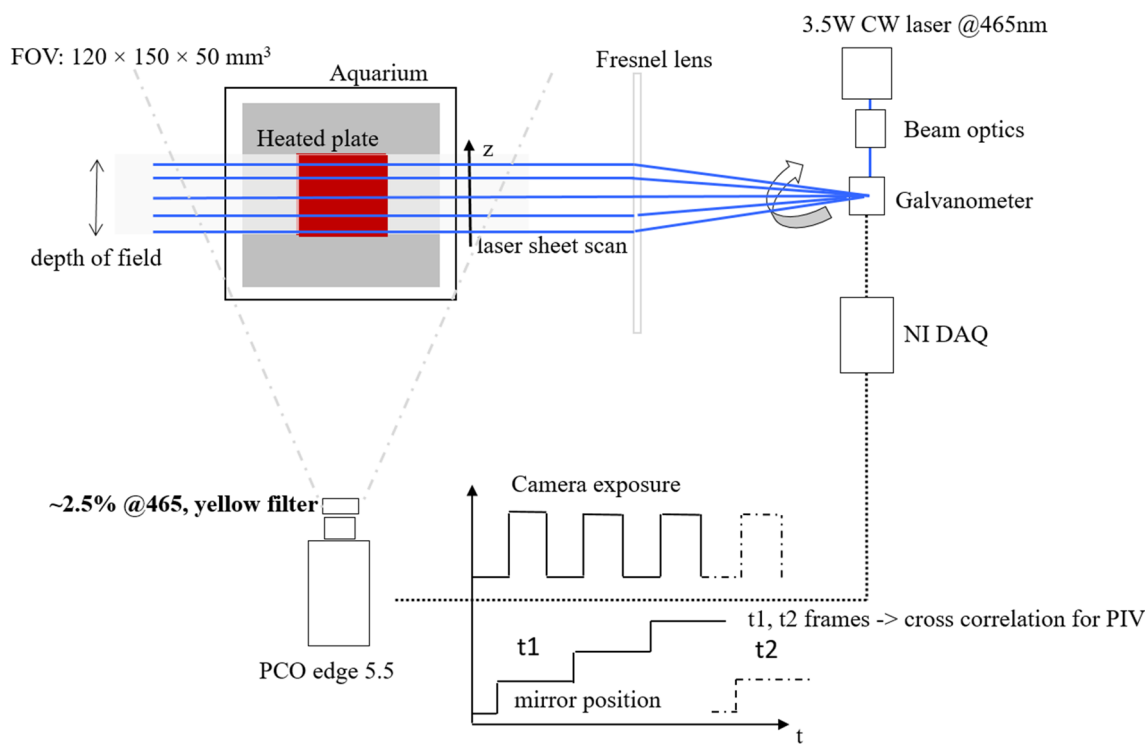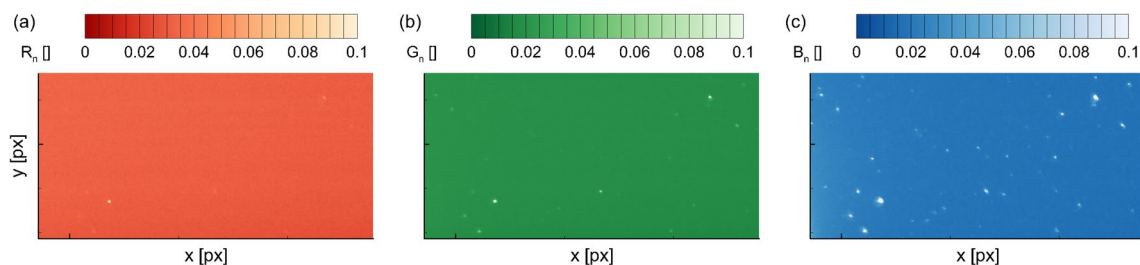

Fig. 4 The single camera PIV–LIF experimental setup

Fig. 5 Examples of raw experimental images: red (**a**), green (**b**), blue(**c**). The intensity has been normalized by the raw counts, i.e., by 2^{16} which is the maximum allowed image intensity
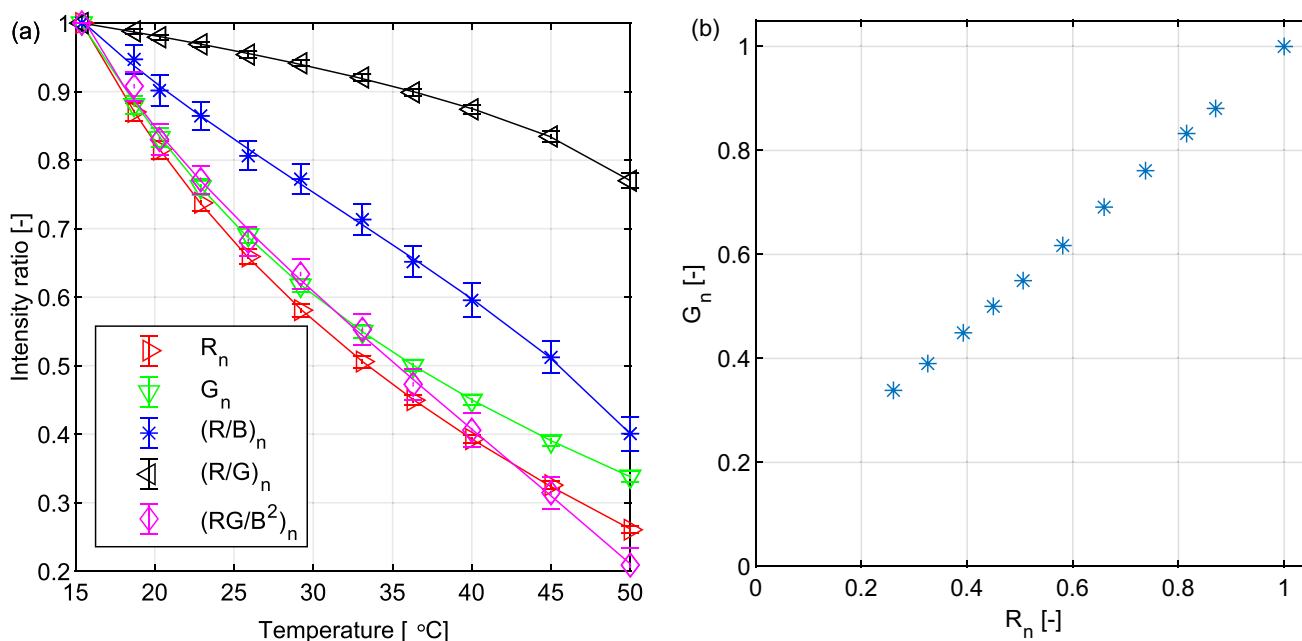
Fig. 6 **a** Temperature calibration of various ratios and **b** correlation of the R and G channels

interpolation between pixels is performed to align the color channels as it is assumed that the spatial gradients in the temperature field are small enough to omit the interpolation scheme without introducing any significant error. This allows us to obtain from the native resolution of 2560×2160 pixels three separate RGB images of size 1280×1080 pixels.

The particle images pairs recorded by the blue channel can be used to compute the velocity field using state-of-the art PIV algorithms (Raffael et al. 2018). As the particle image displacements are analyzed only between sub-images of the same color channel (e.g., the blue channel), the estimates of the displacement remain consistent. The red channel contains mainly the fluorescence signal of RuPhen while the green channel captures a combination of the fluorescence emission of RuPhen and the leakage contribution of the blue-laser Mie scatter. Note that the signature of the PIV tracers can be removed applying a 2D median filter or employing image segmentation, which is computationally more expensive.

A binning operation on 5×5 px kernels is performed on the recordings to improve the signal-to-noise ratio. Beforehand we also perform a dark image subtraction as it is commonly done in LIF. By exploiting the characteristics of the RuPhen dye and spectral sensitivity of the color camera, both the red and green channels are used to obtain the temperature field. For this purpose, we model the intensity of the responses of the red and green channels (I_R and I_G, respectively) as a mixture of the fluorescence emission signal and excitation laser intensity I_0:

$$I_R = I_{fr}(x, y) + w_1 I_0(x, y) \tag{1}$$

$$I_G = I_{fg}(x, y) + w_2 I_0(x, y) \tag{2}$$

where I_{fr}, I_{fg} are the fluorescence signals in the red and green channel, respectively. A simple surface-scatter measurement allows us to determine the contribution of the laser illumination, I_0, on the red and green channels, and to obtain $w_1 = 0.04$ and $w_2 = 0.16$. These values confirm that the red channel mostly captures the fluorescence signal of the RuPhen dye with almost no contribution from the laser. On the other hand, a correction using the blue channel image should be applied to the green channel image to remove the contribution of the laser illumination.

All channel and channel-combination ratios normalized by a reference temperature (i.e., $R_n, G_n, R_n/G_n, R_n G_n/B_n^2$) monotonically decrease with temperature however exhibiting a different sensitivity (Fig. 6). These ratios can be used to derive a calibration curve that relates intensity to temperature.

One of the challenges in LIF is the appearance of intensity fluctuations that are not due to temperature changes. Here, we use color channel ratios (i.e., R_n/G_n or $R_n G_n/B_n^2$) to help correct the effect of the three main sources of error: the non-uniform laser sheet profile, the laser intensity fluctuations, and the (weak) dye absorption. However, the use of the green and blue channels is not ideal due to the leakage contribution of the laser illumination that may ultimately add considerable noise to the temperature fields.
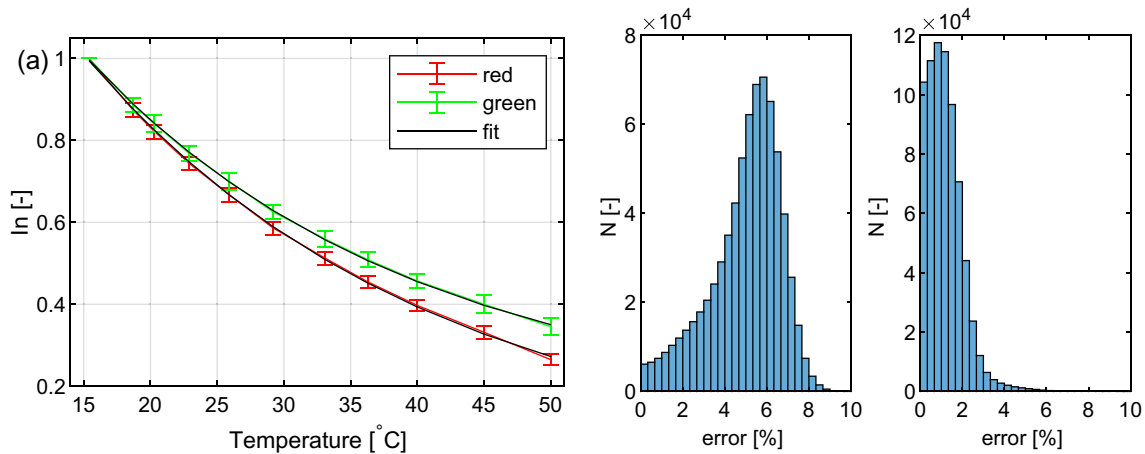
Fig. 7 **a** Temperature calibration curves using normalized red and green channels; **b** the histogram of the bias error; and **c** the corrected histogram after applying laser power correction

As the red and green channels are highly correlated (Fig. 6b), the ratio R_n/G_n displays a lower temperature sensitivity than the other ratios (Fig. 6a). Normalizing the red channel by a reference temperature, i.e., R_n, has the advantage of preserving a high-temperature sensitivity and a clear separation between the fluorescence emission and laser irradiance contributions. Note that R_n still corrects for the non-uniform laser sheet profile and absorption effects.

2.5 Laser power fluctuation correction

The calibration approach requires a method to eliminate the laser illumination fluctuations $I_0(t)$. This is achieved by using the normalized calibration curves of both the red and the green channels (Fig. 7a). We employ a numerical optimization scheme (detailed in Appendix A) that uses the different normalized intensity pairs $\{R_n, G_n\}$ computable for all superpixels, i.e., the 2×2 px unit cells of the RGB Bayer pattern, in any instantaneous image. For each such intensity pair, the dependency on the local temperature $T(x, y)$ is approximated by a parametric fit, specifically two exponential functions:

$$R_n[T(x, y)] = \Gamma \, \alpha_R \, \exp\left[-\beta_R T(x, y)\right] \tag{3}$$

$$G_n[T(x, y)] = \Gamma \, \alpha_G \, \exp\left[-\beta_G T(x, y)\right], \tag{4}$$

where the unknown intensity ratio is modeled as $\Gamma = I_0(t)/I_{0,ref}(t)$, while the fit parameters $\{\alpha_R, \alpha_G, \beta_R, \beta_G\}$ are the same for all superpixels.

Solving the two equations above for the temperature and minimizing the difference between the two estimates obtained from the red and green channels allows us to write a minimization problem in the unknown intensity ratio Γ,

$$\arg\min_{\Gamma} \sum_{x,y} \left[\frac{1}{\beta_R} \ln\left(\frac{R_n}{\Gamma \, \alpha_R}\right) - \frac{1}{\beta_G} \ln\left(\frac{G_n}{\Gamma \, \alpha_G}\right) \right]^2, \tag{5}$$

whose solution is

$$\ln \Gamma = \frac{\beta_R \, \beta_G}{\beta_G - \beta_R} \frac{1}{N_{x,y}} \sum_{x,y} \left[\frac{1}{\beta_R} \ln\left(\frac{R_n}{\alpha_R}\right) - \frac{1}{\beta_G} \ln\left(\frac{G_n}{\alpha_G}\right) \right], \tag{6}$$

where $N_{x,y}$ is the number of superpixels involved in the estimation. Notice that this formulation can be applied to images with arbitrary temperature distributions as it does not explicitly contain the local temperature.

The effects of the correction accounting for the fluctuating laser intensity are shown in Fig. 7. After having corrected for a 10% change in the illumination intensity, the distribution of temperature errors is reduced when reconstructing the calibration data. This estimate of the instantaneous laser intensity is very robust due to the large number of superpixel data used in the minimization problem. Note that the basic approach is independent of the functional shape of the two calibration curves as long as they differ and can be inverted for each temperature value. Furthermore, it has the benefit of preserving the high sensitivity of the RuPhen dye, which may not be possible if a ratiometric approach is chosen (as, for example, in Funatani et al. 2004). The procedure may be applied locally in smaller regions of the intensity map in order to compensate for changes in the light sheet intensity distribution.
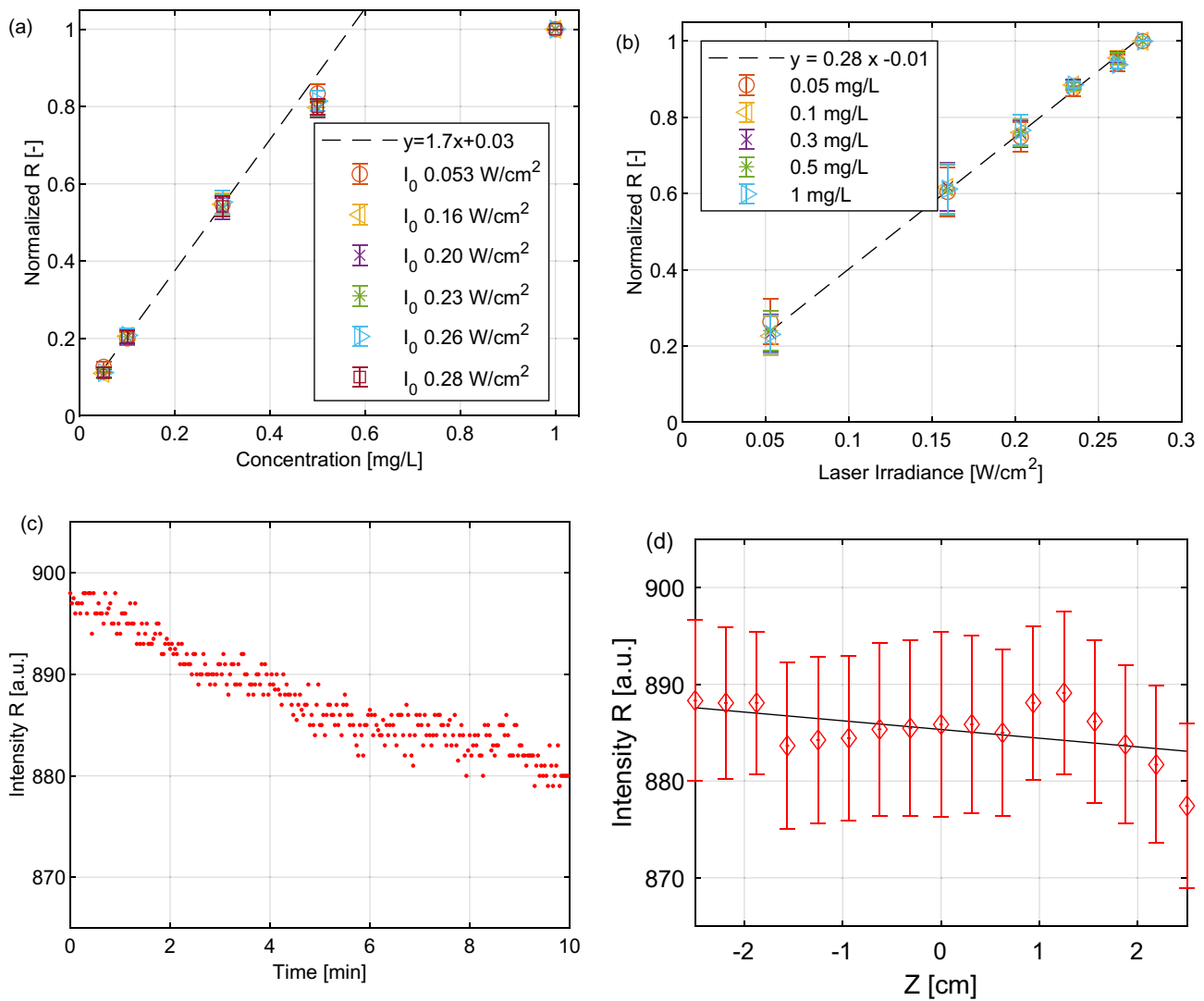
Fig. 8 **a** Normalized fluorescence intensity (using the red channel) versus **a** concentration, **b** laser irradiance I_0, **c** time, and **d** propagation distance

3 Experiments

We demonstrate the ability of our approach to provide simultaneous velocity and temperature measurements by conducting three sets of experiments. First we characterize the performance of the RuPhen dye, then we look at the natural convection generated by a hot surface of finite size, and finally we consider a more complex thermo-fluidic pattern evolving in and around a heated hemisphere in presence of crossflow.

3.1 RuPhen dye characterization

The RuPhen fluorescence response to increasing concentrations and varying laser irradiance, I_0 was systematically

characterized. The fluorescence intensity is normalized by a known reference temperature and plotted in Fig. 8a as a function of dye concentration. At relatively low concentrations (i.e., in the range between 0.05 mg/L and 0.3 mg/L), RuPhen exhibits an approximately linear response to the changes in concentration whereas the response becomes nonlinear at higher concentrations due to Beer absorption/re-absorption effects.

Employing a CW laser as excitation source, the dye response is linear with laser irradiance, I_0, in the weak excitation regime ($I_0 \ll I_{sat}$) for I_0 up to 0.3W/cm^2 (Fig. 8b). RuPhen does not undergo photobleaching (Fig. 8c) or reabsorption along the optical axis (Fig. 8d). A very slight decrease in the fluorescence emission is observed with time (Fig. 8c), which is attributed to a small reduction in laser power due to thermal drift issues when the device
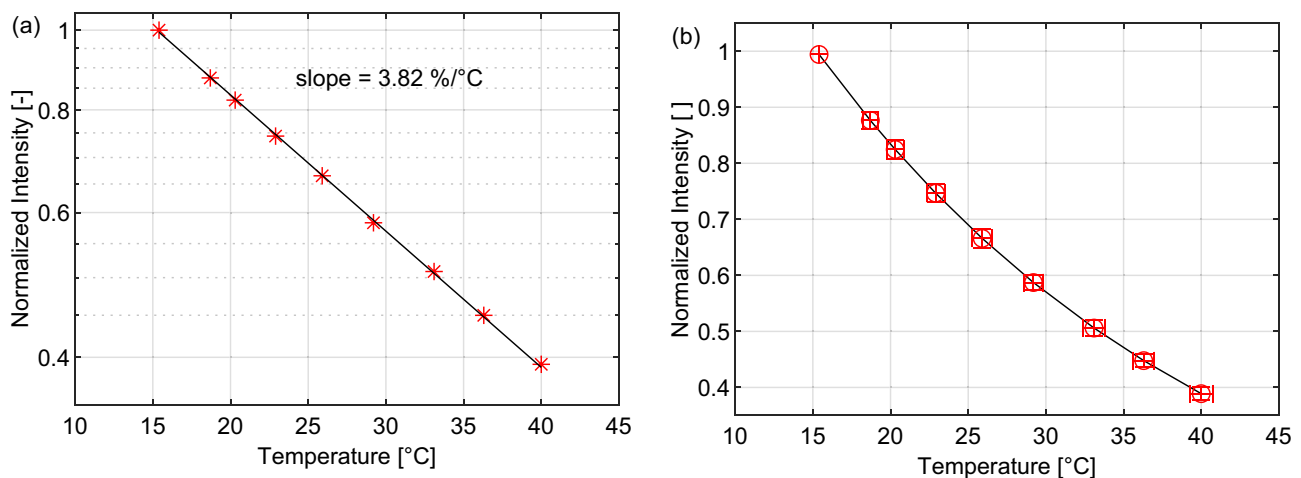
Fig. 9 Calibration curves for the red channel using the model proposed by eq. 3 for the hemisphere experiment Sect. 3.3, obtained by normalizing the data by the intensity recorded at 15°C. Left: logarithmic plot showing a measured sensitivity of 3.8%/°C. Right: calibration curve including error bars at the recorded calibration points

is continuously operated for a long time. We note that the RuPhen solution remained quite stable over months and did not undergo any degradation. The signal-to-noise ratio is high enough to obtain single-shot, time-resolved temperature fields, even when a CW laser is used to excite a low RuPhen concentration to stay within the optically thin system limit (Walker 1987). Figure 9 demonstrates the strong monotonic decrease of fluorescence emission of RuPhen with temperature. Here, we measured in the temperature range between 15 °C and 40 °C, but this interval could be further extended.

Based on the intensity change observed by the camera, the average temperature sensitivity over the whole temperature range was found to be 3.8% °C, which is in very good agreement with the value calculated from the spectrometer measurements, i.e., 4% °C (Fig. 2). When a global calibration is performed by normalizing the data with the recordings at the lower temperature, the average uncertainty on the temperature measurements is 0.5 °C in the range between 15 and 40 °C. The uncertainty can be reduced to 0.3 °C if we use the mean of all calibration points as reference. However, this may not always be feasible in practical applications, as it would require to heat the whole test section or facility uniformly to the mean temperature encountered during the experiment.

For a given concentration, the temperature sensitivity of the dye remains almost constant when the CW laser irradiance, I_0, is varied. This is in agreement with previous studies showing that dyes with temperature dependent quantum yield, $\phi(T)$, lose their temperature sensitivity only if excited in the saturated/partially-saturated excitation limit ($I_0 \gg I_{sat}, I_0 \approx I_{sat}$), which usually implies the use of a pulsed laser source in the mJ range (Chaze et al. 2016).

3.2 Thermal plume

We applied our thermometric approach to measure the three-dimensional (3D) temperature field in a thermal plume above a 50 mm square plate, which was placed in ambient water at T_∞=10 °C and heated (T_h= 50 °C). To stabilize the plate surface temperature, a temperature controller was used along with a T-type thermocouple as a reference and a data logger (Sefram, France). The setup is schematically shown in Fig. 4.

The camera field of view was 12 cm × 15 cm while the depth of field covered 5 cm. The effective sensor size was reduced to 1424px × 1119px, enabling an acquisition frame rate of f_s= 62 Hz for a lens aperture F/2.8 at an exposure time of 10 ms. A RuPhen concentration of 0.1 mg/L (equivalent to a molarity of 1.4d-7 mol/L) was used along with hollow glass spheres (HGS) of diameter $10\mu m$. To obtain a fluorescence signal, which is linearly proportional to the laser irradiance, I_0, the dye was excited in the weak excitation limit where the laser irradiance is much lower than the dye saturation limit ($I_0 \ll I_{sat}$). The light sheet optic was used together with the galvanometer mirror to scan the light sheet in order to extend the technique to 3D-LIF/3D-2-component PIV. The laser produced a maximum measured power of 1.8 W at the output of the optics. Notice that this power level would have been insufficient to provide full volumetric illumination while maintaining a sufficient signal-to-noise ratio in the fluorescence images. (A solution for full volumetric illumination would require a significantly more complex setup consisting of a pulsed laser and several intensified cameras for tomographic reconstruction, see, e.g., Halls et al. (2016) for the case study of a gaseous free jet). The measurements
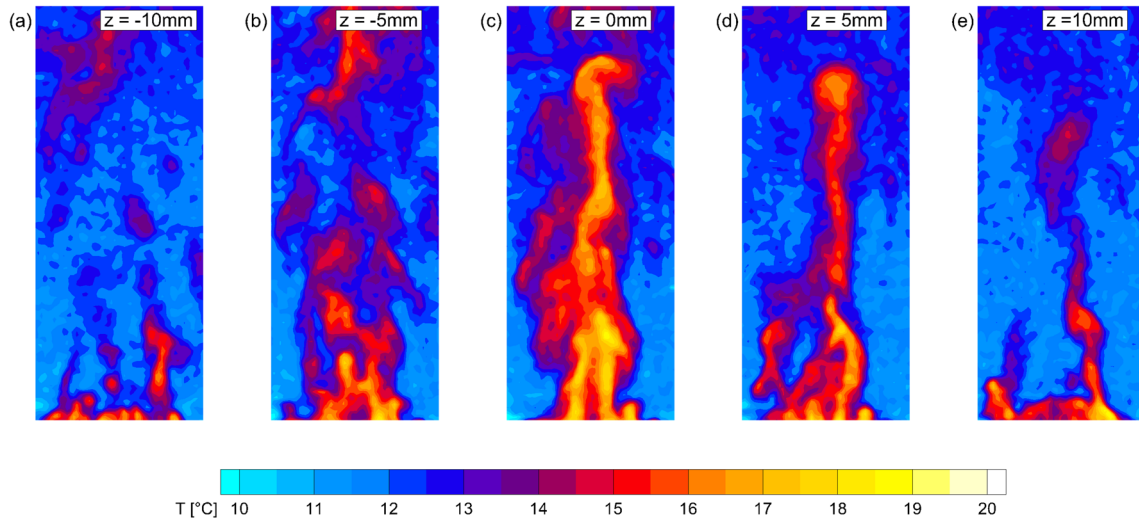
Fig. 10 Snapshots of "single-shot" temperature fields of the turbulent thermal plume obtained at various depths by a scanning laser sheet

were carried out by scanning $N_z = 40$ planes to obtain a sufficient spatial resolution in the depth direction for 3D LIF. With the chosen frame rate a single sweep of the measurement volume took 650 ms.

The LIF calibration is performed in situ by recording uniform temperature images at the same laser irradiance as in the final measurements. The temperature of the water in the aquarium was controlled by means of a heat exchanger connected to a Lauda VC5000 unit. To calculate the temperature field, the red-channel and green-channel pixels are extracted by processing the raw images after subtracting the offset, i.e., the camera dark image and employing a 5×5 binning.

Fig. 11 Left: iso-surfaces of the time-averaged temperature field of the thermal plume at $T = 14°C$, $15°C$, and $16°C$. Right: iso-surfaces of the time-averaged velocity magnitude at 1, 10, and 20 mm/s. Additionally, the plot shows contour maps of the velocity magnitude and velocity vectors on horizontal planes extracted at different heights above the hot plate
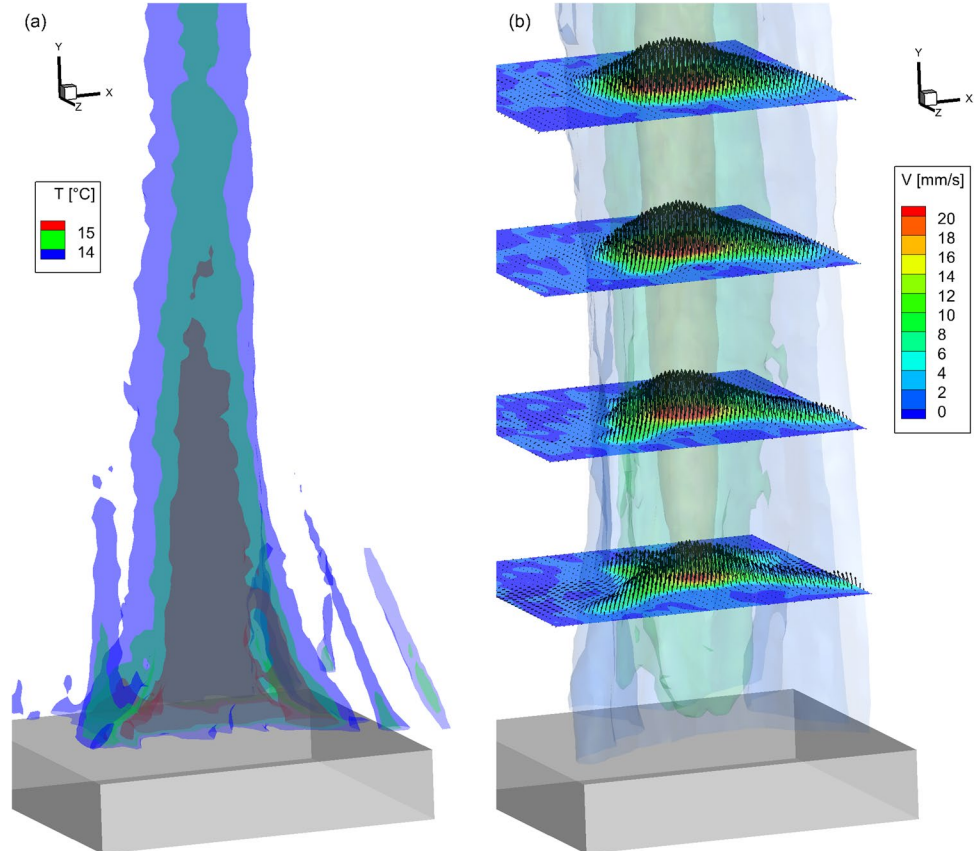
The laser contribution in the green channel is eliminated based on the blue leakage model (Sect. 2.4).

After having eliminated the laser intensity variations, a global calibration is applied to convert the intensity values into temperature.

The 3D, time-averaged velocity field is computed based on a two-step procedure. First, a custom 2D PIV algorithm (64 px × 64 px window size, Whitakker peak interpolation, ensemble correlation averaging) is applied using images of consecutive scan positions. Since the light sheet provides sufficient overlap between positions and the cross-flow velocities are small, proper correlation quality can be maintained. The missing out-of-plane velocity component is then computed in a second step applying the continuity equation (incompressibility condition) and integrating the resulting cross-flow velocity gradient. The spatial resolution of the temperature and flow fields is 0.5 and 1.2 mm, respectively.

Instantaneous temperature fields of the thermal plume for various z-planes are shown in Fig. 10 where the development of the turbulent thermal plume is clearly visible. The frame rate of the camera is high enough to ensure a near "frozen" field condition during a single volume scan of the buoyant plume.

The reconstructed 3D mean temperature and velocity iso-surfaces show distinct coherent structures, especially in the lower part of the turbulent plume (Fig. 11), which demonstrates the efficacy of our method. At heights beyond approximately one heater width the temperature and velocity fields attain an almost columnar structure without significant further changes.

3.3 Heated hemisphere in crossflow

Thermal convection inside a hemisphere is a subject of interest for atmospheric and geophysical flows as well as for heat transfer studies (Meuel et al. 2018; Shiina et al. 1994; Lewandowski et al. 1996). The heated hemisphere has similarities with the classic Rayleigh-Bénard convection in which buoyant thermal plumes lead to the onset of turbulent thermal convection. Here, we specifically aim at quantifying the nature of the coupled flow inside and around the hemisphere for various flow regimes, ranging from natural to forced convection. We simultaneously extract the velocity and temperature fields using the single camera PIV–LIF technique.

The measurements were performed in the refractive index matching (RIM) water tunnel (test section: 15 cm × 15 cm × 38 cm) at the Swiss Federal Laboratories for Material Science and Technology (Empa). The model consisted of a circular heater from Minco (diameter 5 cm, model: HM6970), and a transparent hemispherical shell, which was manufactured by thermoforming a fluorinated ethylene propylene (FEP) sheet of 0.5 mm thickness into the desired dome shape (Fig. 12, bottom left). As FEP has a refractive index (RI = 1.3385), which is very close to water, adding a 5% by wt. glycerol solution was sufficient to match the two RIs. A concentration of 0.2 mg/L (2.8d-7 mol/L) of RuPhen was used as the temperature sensitive fluorescent dye along with hollow glass spheres (HGS, size: $10\mu m$, density: 1.1kg/m^3) as tracers for the PIV measurement.

The measurement setup (Fig. 12, right) consists of the CW laser assembly as the excitation source for RuPhen, with the light sheet pointing upstream in the flow facility, and the camera (single frame, 50 mm lens, aperture F/2.8) that records the side view (i.e., perpendicular to the light sheet).

As before, the Mie scattering of PIV particles is captured in the blue channel, whereas the temperature-dependent fluorescence signal is registered in the red channel of the camera. The calibration was performed in situ at the same laser irradiance as in the final measurements and varying the fluid temperature by means of a thermostat connected to the experimental flume. The velocity field is estimated from the images of the particle position recorded in the blue channel, which are processed by a commercial PIV processing software (DaVis, LaVision) that employs a sum-of-correlation with final interrogation window size of 48 px × 48 px and 75% overlap, and then post-processed using universal outlier detection. To estimate the uncertainty of the vector fields,
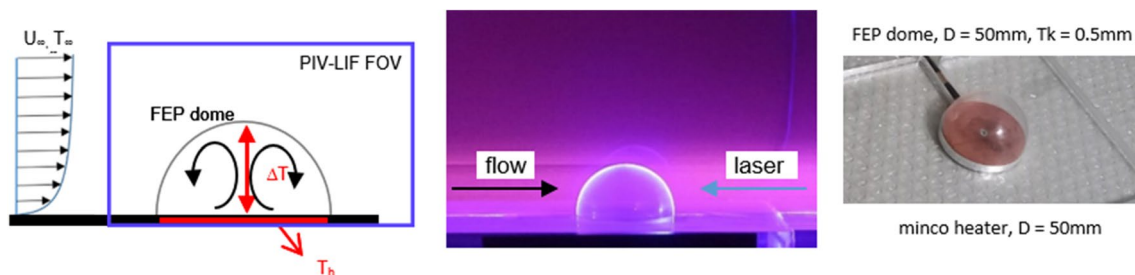

Fig. 12 The experimental setup in the refractive index matching (RIM) water tunnel at the Swiss Federal Laboratories for Material Science and Technology (Empa) and the circular heater/ FEP dome assembly. Notice that the photographs are taken before adding glycerol to the water to match the refractive index of FEP
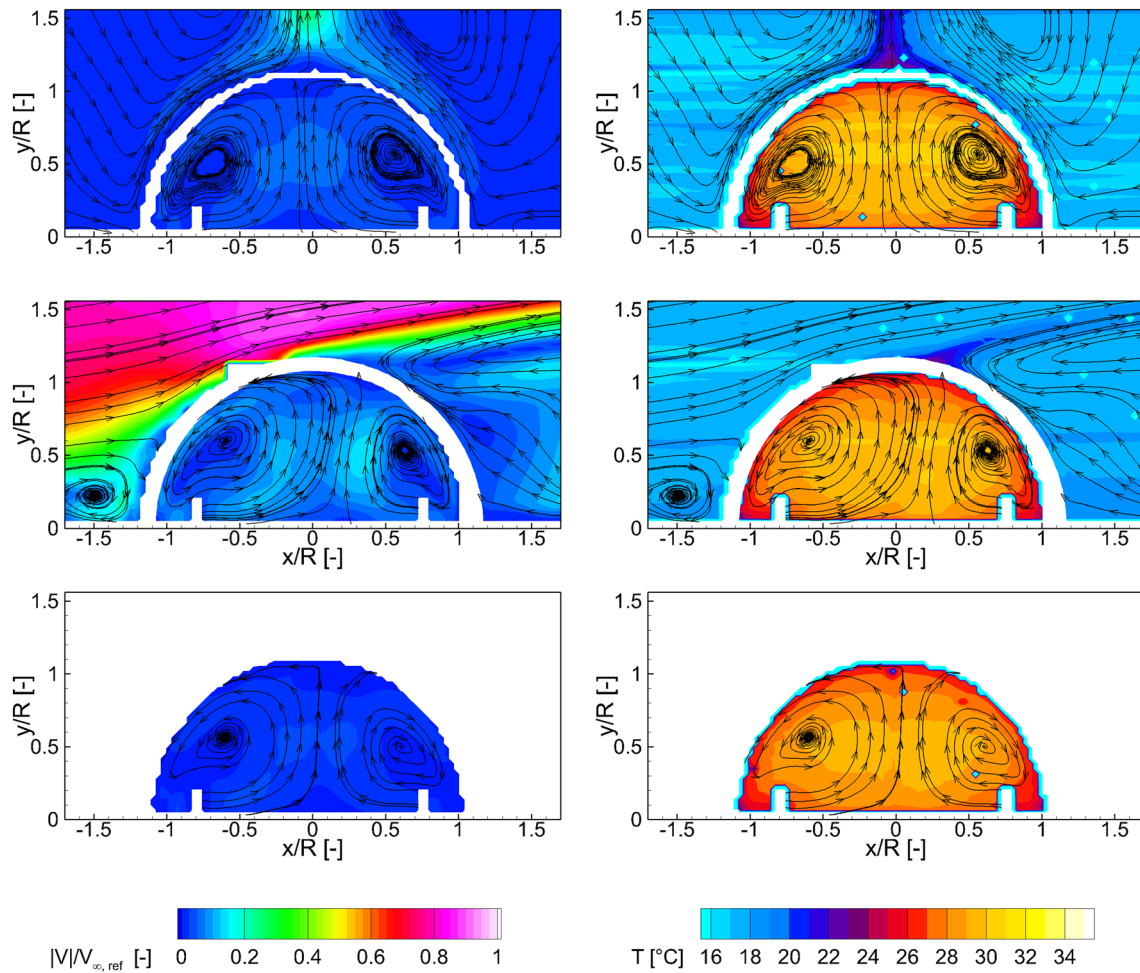
Fig. 13 Time-averaged velocity (left column) and temperature fields (right column) in the case of a hemisphere in cross-flow at different Reynolds and Richardson numbers. From top to bottom rows: natural convection case (Re = 0, Ri = ∞); mixed convection (Re = 1000, Ri = 5.6); and forced convection (Re = 23,750, Ri = 0.01). The velocity fields have been normalized by the convective velocity or the free stream velocity depending on the flow regime

we assume that the sampling error of the average velocity field (defined as $\epsilon = \frac{1}{\sqrt{N}} \frac{u'}{|U|}$) represents the major contributor (see also Armellini et al. 2011; Mucignat et al. 2013). This leads to a relative error of about 1 % in the regions of strong convective motion and about 10 % in the recirculation regions. With the parameters of the optical setup and of the image post processing, we obtain a velocity vector every 0.9 mm and one temperature value every 0.4 mm.

Based on the Reynolds and Richardson numbers obtained with the dome diameter D, the reference velocity, and the temperature outside the dome, we identify three different flow regimes: natural convection, mixed convection, and forced convection. As suggested in other works (Zhang et al. 2018; Acharya 2022), the reference velocity for the natural-convection case is defined as $U_{ref} = \sqrt{g\beta D\Delta T} = 0.055$ m/s. Conversely, for the mixed and forced convection regimes, we

take the free stream velocity as reference velocity (0.04 at $Re = 1000$ and 0.54 m/s at $Re = 23750$, respectively).

The spatial distribution of the time-averaged temperature and velocity fields at mid-plane for the natural ($Re = 0$, $Ri = \infty$), mixed ($Re = 1000$, $Ri = 5.6$), and forced ($Re = 23,750$, $Ri = 0.01$) regimes are shown in Fig. 13, where we have also superimposed the 2D streamlines to facilitate the identification of the flow features. The bulk temperature field measured using LIF is relatively uniform, especially outside the dome, which is in agreement with pointwise thermocouple measurements.

In the case of natural convection (Fig. 13, top row), the streamlines, the velocity, and the temperature fields display a symmetric large-scale recirculation pattern inside the cavity. Outside, the heat flux through the hemisphere outer surface generates a thermal boundary layer and a symmetric plume. In the mixed convection case (Fig. 13, middle row), the velocity field and streamlines indicate the presence of a

small upstream recirculation region, due to the interaction of the upstream boundary layer and the bluff body. This small recirculation might be associated with the development of a horse-shoe vortex. Furthermore, we note the presence of a shear layer that detaches close to the top of the hemisphere and produces the lift-off of the hot fluid layer flowing along the hemisphere leeward side; the associated thermal signature was also well captured by the LIF measurements. Consequently, a large separation on the downstream side of the hemisphere is observed. In the mixed-convection regime, the upstream and downstream heat transfer rates are clearly different, yielding an asymmetric pattern in the large-scale recirculation inside the hemisphere. Interestingly, the large-scale recirculation pattern inside the hemisphere becomes again symmetric in the forced-convection regime (for Ri < 0.01) because the enhanced mixing in the turbulent near wake leads to comparable heat transfer rates in the downstream region. Furthermore, the normalized temperature field inside the hemisphere shows higher temperature gradients compared to the natural- and mixed-convection regimes due to a more effective cooling of the fluid close to the hemisphere inner surfaces.

Remarkably, the method allows us to observe the signature of symmetric or non-symmetric flow topology also in the instantaneous temperature fluctuations T'. Figure 14 reports the space-time plot of T' extracted at $y/D = 0.2$ for the flow regimes as shown in Fig. 13. At Re = 0 and Ri = ∞, both the instantaneous LIF data (Fig. 14a) show the symmetrical development of multiple plumes, which originate from both sides of the plate at $x/R = 0.5$ and move towards the symmetry axis $x/R = 0$. Conversely, in the mixed convection case (Re = 1000, Ri=5.6, Fig. 14b), the plumes released from the leeward side of the plate extend further downstream, up to $x/R = 0.3$. If the free stream velocity is further increased to yield a pure forced convection regime (Re 23750, Ri =0.01) the grade of asymmetry is partially reduced, as shown in Fig. 14 c, and observed previously in Fig. 13.

4 Conclusions

In this study, we proposed and evaluated an experimental setup that employs RuPhen as fluorescent dye, a blue CW diode laser as excitation source, and a single color camera to simultaneously measure temperature and velocity fields. The technique was also extended to 3D by incorporating a scanning light sheet that uses a galvanometer mirror. We demonstrated that a low dye concentration is sufficient because the RuPhen exhibits a strong absorption at 465 nm. By using RuPhen alone but recording its photoluminescence with two-color channels, we were able to avoid the spectral conflicts that arise instead in the ratiometric techniques using
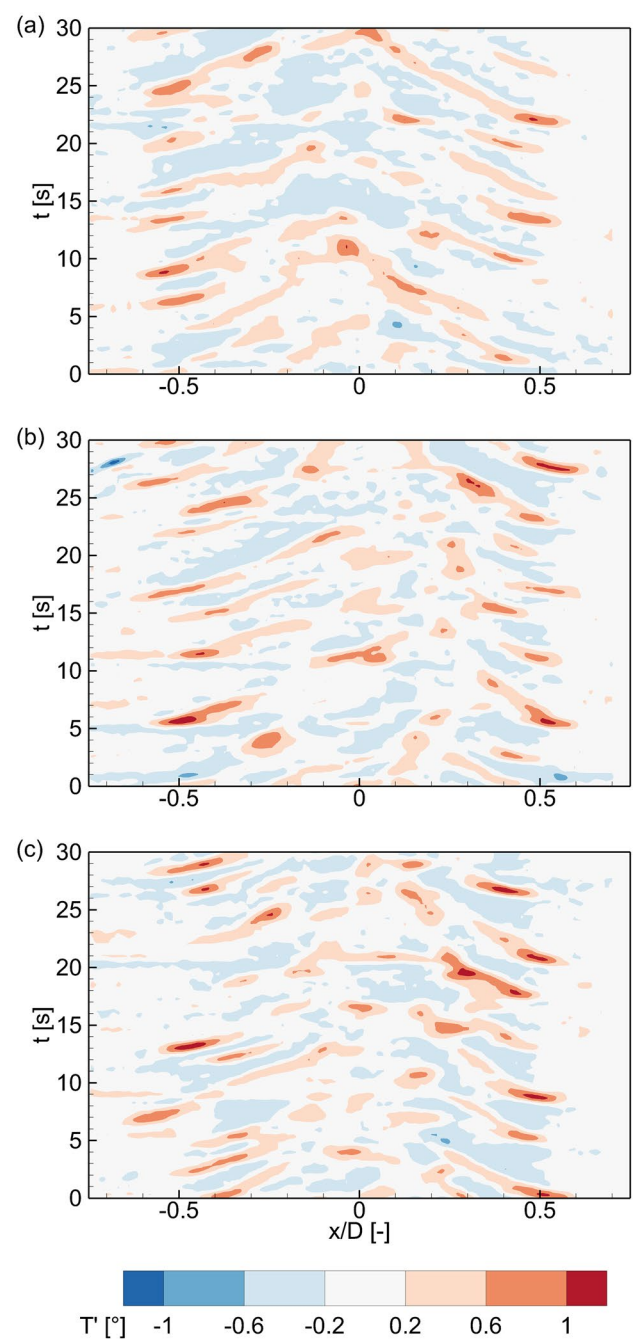

Fig. 14 Space-time plot of the temperature fluctuation T' recorded by LIF. Data are obtained at Ri = ∞ (**a**), Re=1000, Ri = 5.6 (**b**), Re=23,750, Ri = 0.01 (**c**) and position $y/D = 0.2$

more than one dye and, at the same time, achieve a higher temperature sensitivity coefficient (up to 4%/°C), which is comparable to the sensitivity obtained by more complex approaches. The higher sensitivity was achieved by introducing a novel correction that uses the red and green channels to account for laser power fluctuation without resorting to the usual ratiometric approach to eliminate the dependency on

the intensity fluctuations. We observed that the red channel of the color camera can separate quite well the fluorescence emission of the dye from the blue laser irradiance. A limitation of the single color camera technique remains in the extension to 3D measurements due to the so-called aperture problem which leads to a comparatively poor signal-to-noise ratio in the fluorescence signal. Furthermore, the technique is limited by the (currently available) camera frame rate, especially during 3D measurements using the scanned light sheet, and the current lack of the "double frame" mode for PIV recordings. Nevertheless, our method proved to be capable of performing a volumetric reconstruction of convective flows by scanning the domain with a light sheet. Furthermore, it is a cost-effective solution to observe thermal boundary layers, recirculation patterns and flow separation also in complex flow test cases. In particular, due to the overall sensitivity, also consistent measurement of the instantaneous temperature fields can be obtained.

Appendix A: Correction for laser power fluctuations

Consider a camera's signal S, gain G, dark level D, and observed light intensity I as functions of pixel position (x, y), temperature T, and recording time t. We write as a model

$$S(x, y, T, t) = G(x, y)I(x, y, T, t) + D(x, y) \quad (A1)$$

For low concentrations dye absorption can be neglected, and a simplified form for the fluorescence I intensity received by the sensor is given by,

$$I(x, y, T, t) = I_0(t)L(x, y, t)F(x, y, T) \quad (A2)$$

where I_0 is the time dependent laser intensity, $L(x, y, t)$ is the light sheet non-uniformity—which may also include a temporal drift—and F is the fluorescence signal. The intensity ratio of a full camera image w.r.t a recording at uniform reference temperature is then

$$\rho(x, y, T, T_{ref}, t, t_{ref}) = \frac{S(x, y, T, t) - D(x, y)}{S(x, y, T_{ref}, t_{ref}) - D(x, y)} \quad (A3)$$

Substituting Eq. (A2) into Eq. (A3) we get,

$$\rho(x, y, T, T_{ref}, t, t_{ref}) = \frac{I_0(t)L(x, y, t)F(x, y, T)}{I_0(t_{ref})L(x, y, t_{ref})F(x, y, T_{ref})} \quad (A4)$$

The ratio operation eliminates the dependence on the pixel gain $G(x, y)$. The relative red and green signals on separate pixels of the color sensor's Bayer pattern compute accordingly as

$$R_n(x_R, y_R, T, T_{ref}, t, t_{ref}) = \frac{I_0(t)L(x_R, y_R, t)F(x_R, y_R, T)}{I_0(t_{ref})L(x_R, y_R, t_{ref})F(x_R, y_R, T_{ref})} \quad (A5)$$

$$G_n(x_G, y_G, T, T_{ref}, t, t_{ref}) = \frac{I_0(t)L(x_G, y_G, t)F(x_G, y_G, T)}{I_0(t_{ref})L(x_G, y_G, t_{ref})F(x_G, y_G, T_{ref})} \quad (A6)$$

The normalized signals are still dependent on the illumination ratio $\Gamma(x, y, t, t_{ref}) = [I_0(t)L(x, y, t)]/[I_0(t_{ref})L(x, y, t_{ref})]$ between the current and the reference image, which remains unknown in each frame and at every time t. Under the assumption $x_R = x_G$, $y_R = y_G$ the value of Γ will be the same for the red and green channels. Furthermore, if the spatial shape of the light sheet does not change in time, i.e. $L(x, y, t) = L(x, y, t_{ref})$, Γ will be a constant value in each frame at time t.

The value of Γ can be determined by considering multiple measurements with given pairs $\{R_n, G_n\}$ in each recorded frame, e.g., by looking at red-green pixel ratios in small regions or, under the assumption of an unchanging light sheet, the whole image. A model based on generalized calibration curves $r(T)$ and $g(T)$ would give for the ratios

$$R_n = \Gamma\, r(T), \qquad G_n = \Gamma\, g(T) \quad (A7)$$

from which the formal temperature estimates T_R and T_G can be derived by inversion,

$$T_R = r^{-1}\left(\frac{R_n}{\Gamma}\right) \qquad T_G = g^{-1}\left(\frac{G_n}{\Gamma}\right). \quad (A8)$$

Assuming that all the temperatures are *locally* the same, one may postulate

$$T_R = T_G \rightarrow r^{-1}\left(\frac{R_n}{\Gamma}\right) \overset{!}{=} g^{-1}\left(\frac{G_n}{\Gamma}\right) \quad (A9)$$

Given a sufficiently large number of pixel-based values of the red and green channels, the equal temperature criterion can be used to find the best estimate for the *global* or even *local* intensity ratio Γ, using, e.g., a least-squares minimization approach,

$$\sum_{x,y}\left[r^{-1}\left(\frac{R_n}{\Gamma}\right) - g^{-1}\left(\frac{G_n}{\Gamma}\right)\right]^2 \rightarrow min \quad (A10)$$

Considering specifically a simple 2-parameter exponential model for the calibration curves, one can write

$$R_n(T) = \Gamma\, \alpha_R\, \exp\left(-\beta_R T\right) \quad (A11)$$

$$G_n(T) = \Gamma\, \alpha_G\, \exp\left(-\beta_G T\right) \quad (A12)$$

and accordingly

$$T_R = -\frac{1}{\beta_R} \ln \left(\frac{R_n}{\Gamma \alpha_R} \right) \tag{A13}$$

$$T_G = -\frac{1}{\beta_G} \ln \left(\frac{G_n}{\Gamma \alpha_G} \right). \tag{A14}$$

The least squares minimization condition for Γ becomes

$$\mathcal{F}(\Gamma) = \sum_{x,y} \left[\frac{1}{\beta_R} \ln \left(\frac{R_n}{\Gamma \alpha_R} \right) - \frac{1}{\beta_G} \ln \left(\frac{G_n}{\Gamma \alpha_G} \right) \right]^2 \to min \tag{A15}$$

Postulating $\partial \mathcal{F}(\Gamma)/\partial \Gamma = 0$ and expanding the logarithms gives

$$\frac{2}{\Gamma} \left(\frac{1}{\beta_R} - \frac{1}{\beta_G} \right) \sum_{x,y} \left[\frac{1}{\beta_R} \ln \left(\frac{R_n}{\alpha_R} \right) - \frac{1}{\beta_G} \ln \left(\frac{G_n}{\alpha_G} \right) - \left(\frac{1}{\beta_R} - \frac{1}{\beta_G} \right) \ln \Gamma \right] = 0 \tag{A16}$$

With both, $\Gamma \neq 0$ and $\beta_R \neq \beta_G$, this can be further transformed into an explicit solution for Γ,

$$\ln \Gamma = \frac{\beta_R \beta_G}{\beta_G - \beta_R} \frac{1}{N_{x,y}} \sum_{x,y} \left[\frac{1}{\beta_R} \ln \left(\frac{R_n}{\alpha_R} \right) - \frac{1}{\beta_G} \ln \left(\frac{G_n}{\alpha_G} \right) \right] \tag{A17}$$

The global or local value for Γ can then be used to correct for the intensity dependence in the fluorescence signals and to compute the temperature T from the ratio R_n alone—see Eq. (A13) - which is the most reliable measurement.

Note that Γ can be derived independent of the actual local temperature, only a sufficient number of ratio pairs $\{R_n, G_n\}$ is required. Thus, it can be obtained also for single-shot images wherein different temperatures may be present in the region of interest that is being evaluated. The restriction is only the assumption of a locally constant estimate of Γ.

In the case of the RuPhen dye, the calibration curves of normalized red and green responses are shown in Fig. 7a. Assuming a 10% variation in the laser power during the measurements, the uncorrected temperature estimate is shown in Fig. 7b, and the result after applying the above global correction model using the R and G channels is shown in Fig. 7c.

Declarations

Conflict of interest The authors have no competing interests.

Ethical approval Not applicable.

References

Abram C, Pougin M, Beyrau F (2016) Temperature field measurements in liquids using ZnO thermographic phosphor tracer particles. Exp Fluids 57(7):1–14. https://doi.org/10.1007/s00348-016-2200-2

Acharya S (2022) Natural convection heat transfer from upward, downward, and sideward solid/hollow hemispheres. J Thermophys Heat Transfer 36(1):141–153. https://doi.org/10.2514/1.T6273

Armellini A, Casarsa L, Mucignat C (2011) Flow field analysis inside a gas turbine trailing edge cooling channel under static and rotating conditions. Int J Heat Fluid Flow. https://doi.org/10.1016/j.ijheatfluidflow.2011.09.007

Cellini F, Peterson SD, Porfiri M (2017) Flow velocity and temperature sensing using thermosensitive fluorescent polymer seed particles in water. Int J Smart Nano Mater 8(4):232–252. https://doi.org/10.1080/19475411.2017.1409822

Chaze W, Caballina O, Castanet G, Lemoine F (2016) The saturation of the fluorescence and its consequences for laser-induced fluorescence thermometry in liquid flows. Exp Fluids. https://doi.org/10.1007/s00348-016-2142-8

Coppeta J, Rogers C (1998) Dual emission laser induced fluorescence for direct planar scalar behavior measurements. Exp Fluids 25:1–15. https://doi.org/10.1007/s003480050202

Crimaldi JP (2008) Planar laser induced fluorescence in aqueous flows. Exp Fluids 44:851–863. https://doi.org/10.1007/s00348-008-0496-2

Dabiri D (2009) Digital particle image thermometry/velocimetry: a review. Exp Fluids 46(2):191–241. https://doi.org/10.1007/s00348-008-0590-5

Fujisawa N, Funatani S, Katoh N (2005) Scanning liquid-crystal thermometry and stereo velocimetry for simultaneous three-dimensional measurement of temperature and velocity field in a

turbulent Rayleigh-Bénard convection. Exp Fluids 38(3):291–303. https://doi.org/10.1007/s00348-004-0891-2

Funatani S, Fujisawa N, Ikeda H (2004) Simultaneous measurement of temperature and velocity using two-colour LIF combined with PIV with a colour CCD camera and its application to the turbulent buoyant plume. Meas Sci Technol 15(5):983. https://doi.org/10.1088/0957-0233/15/5/030

Halls BR, Thul DJ, Michaelis D, Roy S, Meyer TR, Gord JR (2016) Single-shot, volumetrically illuminated, three-dimensional, tomographic laser-induced-fluorescence imaging in a gaseous free jet. Opt Express 24(9):10040–10049. https://doi.org/10.1364/OE.24.010040

Lam H, Kostov Y, Tolosa L, Falk S, Rao G (2012) A high-resolution non-contact fluorescence-based temperature sensor for neonatal care. Meas Sci Technol 23(3):035104. https://doi.org/10.1088/0957-0233/23/3/035104

Lavieille P, Lemoine F, Lavergne G, Virepinte JF, Lebouché M (2000) Temperature measurements on droplets in monodisperse stream using laser-induced fluorescence. Exp Fluids 29(5):429–437. https://doi.org/10.1007/s003480000109

Lewandowski WM, Kubski P, Khubeiz JM, Bieszk H, Wilczewski T, Szymański S (1996) Theoretical and experimental study of natural convection heat transfer from isothermal hemisphere. Int J Heat Mass Transf 40(1):101–109. https://doi.org/10.1016/S0017-9310(96)00075-0

Massing J, Kaden D, Kähler C, Cierpka C (2016) Luminescent two-color tracer particles for simultaneous velocity and temperature measurements in microfluidics. Meas Sci Technol 27(11):115301. https://doi.org/10.1088/0957-0233/27/11/115301

Massing J, Kähler C, Cierpka C (2018) A volumetric temperature and velocity measurement technique for microfluidics based on luminescence lifetime imaging. Exp Fluids 59:1–13. https://doi.org/10.1007/s00348-018-2616-y

Meuel T, Coudert M, Fischer P, Bruneau C-H, Kellay H (2018) Effects of rotation on temperature fluctuations in turbulent thermal convection on a hemisphere. Sci Rep 8(1):1–7. https://doi.org/10.1038/s41598-018-34782-0

Mucignat C, Armellini A, Casarsa L (2013) Flow field analysis inside a gas turbine trailing edge cooling channel under static and rotating conditions: effect of ribs. Int J Heat Fluid Flow 42:236–250. https://doi.org/10.1016/j.ijheatfluidflow.2013.03.008

Raffael M, Willert C, Scarano F, Kähler CJ, Wereley ST, Kompenhans J (2018) Particle image velocimetry (the Third Edition), 3rd edn. Springer, Berlin. https://doi.org/10.1007/978-3-540-72308-0

Shah J, Allegrini J, Carmeliet J (2018) Ratiometric-2dye-LIF using non-toxic dyes for temperature measurements in large-scale water tunnels. In: Proceedings of the 19th international symposium on application of laser and imaging techniques to fluid mechanics. Lisbon, Portugal. ISBN: 978-989-20-9177-8

Shiina Y, Fujimura K, Kunugi T, Akino N (1994) Natural convection in a hemispherical enclosure heated from below. Int J Heat Mass Transf 37(11):1605–1617. https://doi.org/10.1016/0017-9310(94)90176-7

Tagawa M, Nagaya S, Ohta Y (2001) Simultaneous measurement of velocity and temperature in high-temperature turbulent flows: a combination of LDV and a three-wire temperature probe. Exp Fluids 30(2):143–152. https://doi.org/10.1007/s003480000149

Vogt J, Stephan P (2012) Using microencapsulated fluorescent dyes for simultaneous measurement of temperature and velocity fields. Meas Sci Technol 23(10):105306. https://doi.org/10.1088/0957-0233/23/10/105306

Walker DA (1987) A fluorescence technique for measurement of concentration in mixing liquids. J Phys E Sci Instrum. https://doi.org/10.1088/0022-3735/20/2/019

Wang XD, Wolfbeis OS, Meier RJ (2013) Luminescent probes and sensors for temperature. Chem Soc Rev 42(19):7834–7869. https://doi.org/10.1039/c3cs60102a

Westerweel J (1997) Fundamentals of digital particle image velocimetry. Meas Sci Technol 8(12):1379. https://doi.org/10.1088/0957-0233/8/12/002

Yarin F (2007) Tropea: handbook of experimental fluid dynamics

Zhang J, Liu J, Lu W (2018) Study on laminar natural convection heat transfer from a hemisphere with uniform heat flux surface. J Therm Sci 28(2):232–245. https://doi.org/10.1007/s11630-018-1051-y

Zähringer K (2014) The use of vitamins as tracer dyes for laser-induced fluorescence in liquid flow applications. Exp Fluids. https://doi.org/10.1007/s00348-014-1712-x